Effects of Polarization on Particle-Laden Flows

Jari Kolehmainen,[*] Ali Ozel, Yile Gu, Troy Shinbrot, and Sankaran Sundaresan
Department of Chemical and Biological Engineering, Princeton University, Olden Street, Princeton, New Jersey 08544, USA

Simulations of particle-laden flow with dielectric particles are carried out with varying levels of electrical charging and particle polarization. Simulation results reveal three distinct flow regions. For low particle charge and polarizability, flow is nearly symmetric and nonmeandering. For strong charging and polarization, particles form a continuous and tightly clustered sheet close to one of the walls. Between these extremes, particles form localized particle-rich regions, around which the gas executes a meandering flow. These results indicate that polarization can lead to qualitative changes in the characteristics of particle-laden flows subject to tribocharging.

In this Letter, we examine the effects of particle polarizability on particle-laden flow dynamics. We find that including polarizability produces new and distinct flow regimes in contrast to prior studies that have neglected polarization and consider only neutral or electrically charged particles [1–10]. Since the most pronounced effects of electrical charge are seen in insulating materials and since insulating materials tend to polarize, the study of the effects of polarization is relevant not only to flow and particle elutriation characteristics in gas-fluidized beds of particles [11,12], but also to a broad range of other applications involving charging of insulators.

For example, terrestrial and extraterrestrial dust devils involve insulating materials that charge strongly [13–15], as do mineral dust aerosols [16]. In industrial applications, likewise, spontaneous self-organization associated with particle charging has been reported in microelectronic manufacturing [17] as well as in structural evolution in carbon nanotubes [18,19]. Furthermore, in polyethylene-fluidized bed reactors, particle charging has been linked to particles adhering on reactor walls, known as sheeting [20,21], which causes costly reactor shutdowns and is an ongoing issue in polymer production [22]. Furthermore, there has recently been rapid growth in new applications involving charged insulators, such as triboelectric nano-generators that have been proposed for renewable energy production [23]. Many of these applications involve insulating materials, and findings of this Letter may be germane.

In previous work, Siu et al. [24] investigated the behavior of granular materials in strong electric fields. They found that applied fields can cause particles to produce novel behaviors ranging from static columns to moving ribbons that are not explained by static charges alone. An experimental study of LaMarche et al. [25] also showed that the electric field created by a tribocharged

Teflon sheet is enough to cause significant dielectrophoretic interactions, and suggested that triboelectrification present in granular flows could lead to similar effects. Furthermore, a recent article by Lee et al. [26] investigated clustering of triboelectrically charged particles during free fall in vacuum and concluded that dielectrophoresis associated with particle charges plays an important role in particle dynamics and agglomerate formation. In addition, recent fluidization experiments by Fotovat et al. [11,12] revealed weaker entrainment with insulating particles than with conducting particles having otherwise similar particle properties, reinforcing the view that more comprehensive study of particle polarization is merited. Intriguingly, Feng [27] has even reported that complex electrostatic interactions can cause like-charged dielectric particles to attract one another.

In this Letter, we quantify effects of particle polarizability on dynamics of gas-solid flows by simulating a simple vertical periodic channel, where dielectric particles are fluidized by an upward ambient fluid flow against downward gravity. As we will show, dielectric influences produce distinct flow regimes that would not be seen by considering Coulomb forces alone.

We simulate a fluidized bed with periodic boundaries in the vertical and in one horizontal direction; in the remaining horizontal direction we fix conducting impermeable walls. The driving gas pressure drop ΔP_g, in the vertical direction that supports the particles is adjusted to keep the mean vertical solids flux zero in all simulations. In this Letter, we present simulation results for spherical particles with diameter $d_p = 150 \ \mu m$. The channel is square in cross section, with dimensions $30d_p \times 30d_p \times 120d_p$, and the domain-averaged solid fraction $\langle \phi_s \rangle = 0.1$.

Triboelectrification occurs when a particle collides with other particles or with the channel walls. The triboelectric charging is modeled by following Laurentie et al. [28], in

which the charge transfer is driven by a difference in the effective work function φ that depends on the materials under consideration and the electrical potential difference between the contacting surfaces. This charging model has been found to capture particle charging in a granular chute [29] and in a vibrated granular bed [28,30]. In this model, the effective work function is a lumped parameter that can be determined either empirically [28] or using density functional theory [29].

In the present study, all particles are made of the same material, while the wall is made of a different material so that there is an effective work function difference $\Delta\varphi$ between the particles and wall. The maximum charge that a particle may obtain during a collision with the wall, referred to as the equilibrium charge q_{eq}, can be related to the effective work function difference by $q_{\mathrm{eq}} = \frac{1}{2}\pi\varepsilon_0\Delta\varphi d_p^2/(\delta_c e^+)$ [10]. Here, ε_0 is the vacuum permittivity, δ_c is the electron tunneling distance (taken to be 500 nm in this study), and $e^+ > 0$ is the elementary charge. We characterize the extent of Coulombic interactions using the nondimensional number $e/g \propto \Delta\varphi^2$, a shorthand for the ratio of the Coulomb forces at the contact between particles with charges $\pm q_{\mathrm{eq}}$ to the weight of a particle, $m_p g$ (for details, see Supplemental Material [31]).

We model the induced polarization on particles by applying a simple dielectric polarization law: $\boldsymbol{P} = \varepsilon_0\chi\boldsymbol{E}$, where $\boldsymbol{P}$ is the polarization density, $\boldsymbol{E}$ is the electric field, and χ is the particle susceptibility. The electric dipole moment $\boldsymbol{p}$ of a particle is then $\boldsymbol{p} = \int_{V_p}\boldsymbol{p}\,dV \approx \varepsilon_0\alpha_p V_p\boldsymbol{E}$, where α_p is the (dimensionless) polarizability of the particle and V_p is its volume. In this way, particle charges are governed by the wall-particle work function difference $\Delta\varphi$, and polarization is governed by the polarizability α_p.

Particle and fluid dynamics are solved using an Euler-Lagrange approach, where the locally averaged equations of motion for the fluid phase are solved in an Eulerian framework and the particles are tracked in a Lagrangian fashion by solving Newton's equations of motion [40]. Particle collisions are modeled with a Hertzian contact model [41], and the drag force is accounted for by Wen and Yu's empirical drag law [42]. Electrostatic interactions between particles are modeled using a particle-particle particle-mesh method that accounts for both short-range and long-range effects [43]. Details of the numerical scheme are given in the Supplemental Material [31]. At the nonperiodic walls described earlier, we impose no slip boundary conditions for the fluid, and the electrical potential is fixed at zero. The simulations include both frictional and inelastic particle-wall interactions. At the start of each simulation, the particles are distributed randomly in the simulation domain.

In the results presented here, we vary the e/g value between 0 and 7 (27 different values), while α_p is varied between 0 and 3 (13 different values), producing a total of 339 simulations, each using 20 626 particles. The system
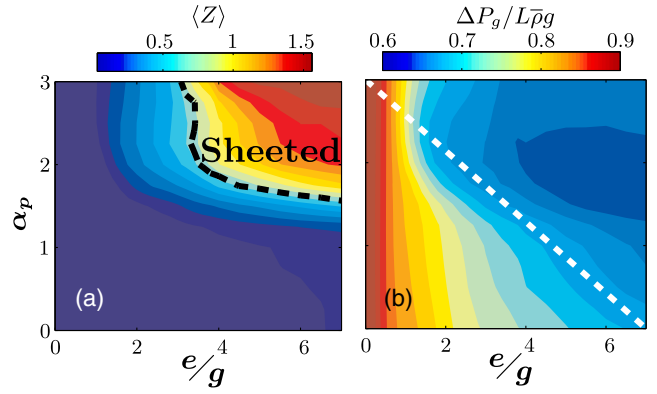

FIG. 1. (a) Mean particle contact coordination number $\langle Z \rangle$ (number of particles contacting a given particle), as a function of the dimensionless ratio of Coulombic and gravitational forces (e/g) and polarizability (α_p). The black dashed line shows contour where average particle contact number $\langle Z \rangle = 0.8$. (b) Driving gas pressure difference normalized by the suspension weight [$\bar{\rho}g = (\langle\phi_s\rangle\rho_p + \langle 1 - \phi_s\rangle\rho_g)g$]. White line, see caption of Fig. 2. Contour plots have been smoothed and interpolated from the actual simulation values, which can be found from the Supplemental Material [31].

charge saturated typically within ~2 s and every simulation was run for an additional 8 s to obtain time-averaged statistics.

Simulation results are summarized in Fig. 1, with panels (a) and (b) showing the average particle contact coordination number $\langle Z \rangle$ and the scaled gas pressure drop, respectively. Higher $\langle Z \rangle$ values, indicative of a more clustered state of the particles, appear when both e/g and α_p are large. We note that without polarizability ($\alpha_p = 0$), strong clustering does not occur for any level of particle charging: a straightforward consequence of Coulomb repulsion. Likewise without particle charging ($e/g = 0$), there are no electrostatic forces irrespective of polarizability, so both particle charging (e/g) and polarizability (α_p) are needed to generate clustering. As we will see, sheeting of particles along a boundary wall occurs in the "sheeted" region of high e/g and α_p, delineated by black broken lines in Fig. 1(a).

As we have described, the simulations use a "laboratory frame" in which particle flux is zero, and the weight of the particles is supported by a combination of gas pressure drop and wall friction. The scaled gas pressure drop, $\Delta P_g/L\bar{\rho}g$, for various combinations of e/g and α_p values [corresponding to Fig. 1(a)] are presented in the form of a contour plot in Fig. 1(b), where $\Delta P_g/L\bar{\rho}g = 1$ implies that the weight of the particles is completely supported by the gas. As the electrostatic forces (Coulombic or dielectrophoretic) increase, the particles become increasingly supported by wall resistance. At low e/g values, the extent of particle charging is small and so the strength of the prevailing electric field is small as well; polarization has a negligible effect under these conditions. As e/g increases polarization plays an increasingly important role.
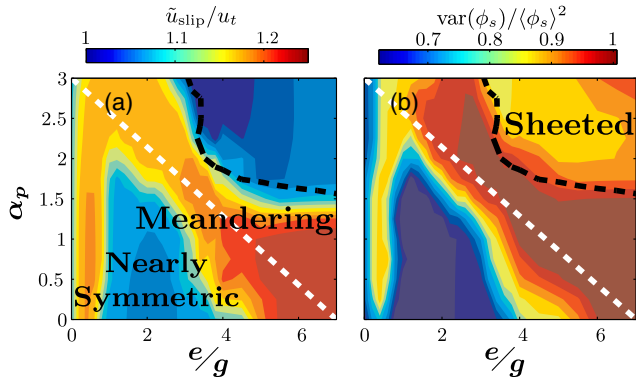
FIG. 2. Flow behavior of nearly symmetric, meandering, and sheeted regions as a function of the dimensionless ratio of Coulombic and gravitational forces (e/g) and polarizability (α_p). (a) Color coding represents the domain-averaged slip velocity ($\tilde{u}_{\text{slip}} = \tilde{u}_{g,z} - \tilde{u}_{p,z}$) normalized by the particle terminal velocity $u_t = 0.432$ m/s. Here, $\tilde{u}_{g,z}$ denotes the Favre-averaged gas velocity, and $\tilde{u}_{p,z}$ denotes the average velocity of all the particles in the domain. (b) Domain-averaged variance of the Eulerian particle volume fraction field (for Eulerian grid size $3d_p$). The black dashed line shows contour where the average particle contact number $\langle Z \rangle = 0.8$ [refer to 1(a)], and the white dashed line identifies both the fastest slip between particles and fluid and the highest variability in particle concentrations. Contour plots have been smoothed and interpolated from the actual simulation values, which can be found from the Supplemental Material [31].

The domain-averaged gas-particle slip velocity, $\tilde{u}_{\text{slip}} = \tilde{u}_{g,z} - \tilde{u}_{p,z}$, presented in Fig. 2(a) manifests a more complex dependence on e/g and polarizability than the contact coordination number and pressure drop shown in Fig. 1. The low contact number region in Fig. 1(a) contains two subregions: one with higher slip velocity and meandering flow pattern [see Fig. 3(a)] and one with lower slip velocity, exhibiting nearly symmetric, nonmeandering flow. In the higher contact number region of Fig. 1(a) ("sheeted"), the average slip velocity is low.

As shown in Fig. 2(b), the distribution of particles in the flow channel is inhomogeneous to some extent even in the absence of electrostatic effects (i.e., near $e/g = \alpha_p = 0$). From an examination of snapshots of simulations [cf. Figs. 3(a) and 3(b)], it appears that this inhomogeneity is associated with a slight enrichment of particles in the vicinity of the walls and the flow-induced dynamic clusters where the particles congregate near each other. Both contribute to particle volume fraction variance, which is nonzero even in the absence of electrostatic effects [see Fig. 2(b)]. They weaken the gas-particle interaction (i.e., the effective drag coefficient) and increase the gas flow rate required to produce the pressure drop needed to maintain zero particle mass flux. Indeed, the average slip velocity [Fig. 2(a)] is in excess of the terminal settling velocity of the particle even though the gas is not required to support the entire weight of the particle.
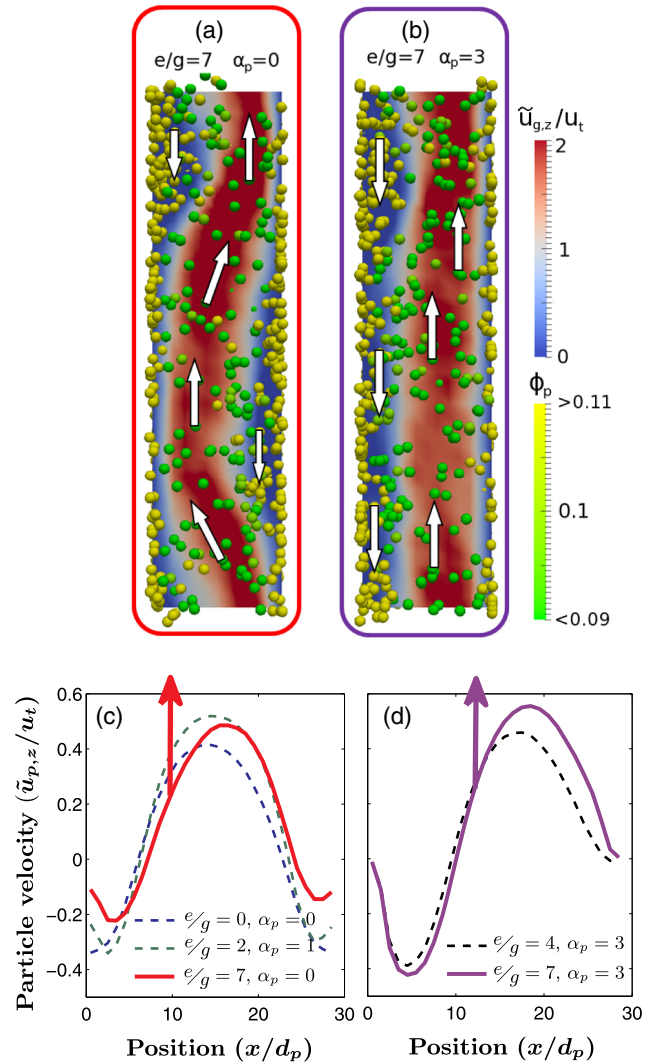

FIG. 3. (a) Snapshot taken after 7.5 s of simulation time from $e/g = 7$ and $\alpha_p = 0$ (no polarization). Background color shows vertical fluid velocity, and particles show the local volume fraction. Yellow (green) particles have local volume fraction above (below) the average volume fraction ($\langle \phi_p \rangle = 0.1$) and on an average tend to move downward (upward). Only every 20th particle is shown and they are magnified to 2.5 times their actual size for ease of visualization. White arrows identify the particle flow directions. Some particles appear outside the channel due to image perspective. (b) The same plot as in panel (a), but for $\alpha_p = 3$ (largest amount of polarization). (c) Time-averaged vertical particle velocity profile for nonsheeted flow configurations. (d) Vertical particle velocity profile for the sheeted flow configuration. Solid red and purple lines show the profile for panel (a) and (b) flows, respectively. Velocity profiles are normalized by particle terminal velocity: $u_t = 0.432$ m/s. The flow patterns illustrated in the snapshots shown in panels (a) and (b) persist in time (see Supplemental Material [31]).

When electrostatic effects are included, a number of changes occur. First, stronger particle-wall interactions lower the pressure drop required to support the particles [Fig. 1(b)]. Second, both the particle volume fraction

variance [Fig. 2(b)] and the required slip velocity to maintain zero particle mass flux [Fig. 2(a)] vary with e/g and α_p in a complex, but largely similar fashion [Figs. 2(a) and 2(b)]. The Pearson correlation coefficient between the slip velocity and the product of particle volume fraction variance and the pressure drop is 0.86, indicating a strong correlation. This similarity can be understood by noting that the average slip velocity is a measure of the ratio between the pressure gradient and the average drag coefficient. Since the average drag coefficient decreases with an increasing particle volume fraction variance, it stands to reason that slip velocity and volume fraction variance should be correlated.

To understand how both slip velocity and volume fraction variance depend on electrostatics, we note that introducing Coulombic interactions (in the absence of polarization) can be expected to cause particle-particle repulsion and wall-particle attraction. Stronger wall-particle attraction in turn draws particles closer to the walls and so lowers the required pressure drop, as illustrated by Fig. 1(b). This same migration of particles toward the walls increases particle volume fraction variance. Working against this effect, Coulombic repulsion between the particles reduces clustering which lowers the variance. The consequence of these competing effects is seen in Fig. 2(b). Increasing e/g first decreases the variance corresponding to increased Coulombic repulsion between particles; a further increase in e/g leads to a large increase in the variance due to enhanced lateral segregation.

Our simulations at low e/g values (and no polarization) did not reveal meandering flow, but a meandering flow pattern as illustrated in Fig. 3(a) is observed above a threshold value of e/g. A meandering flow pattern is accompanied by a large increase in the variance of particle volume fraction, setting up a path of low resistance for the gas to flow through; as a result, the average slip velocity increases when meandering sets in. These are seen clearly in Figs. 2(a) and 2(b). The time-average particle flux in such a state is still nearly symmetric [see solid line in Fig. 3(c)].

Stipulation of periodic boundary conditions in the axial direction influences the threshold e/g value at which meandering sets in. Simulations performed in taller periodic domains produce an onset of meandering flow at lower e/g values (not shown). In fact, a simulation in a periodic domain that is twice as tall yielded a meandering flow even in the absence of electrostatic effects. Thus, including Coulombic interactions lowers the critical axial wavelengths above which meandering flow is obtained, and intensifies the prevalence of meandering flow structures. Simulations performed in wider channels, not shown, manifest analogous trends.

Including polarization changes the flow behavior appreciably. First, the dipoles induced by the electric field give rise to an attractive interaction between particles. It is known that even when particles carry the same charge, strong dipole interaction can lead to a net attractive force between particles [26,27]. As a result, the average contact coordination number tends to increase with an increasing polarizability [see Fig. 1(a)]. Our simulations show that a meandering flow sets in at lower e/g values when polarizability is included. Thus, meandering flows can be expected to be more prevalent in the case of dielectric particles.

Increasing particle charging (e/g) increases the magnitude of the electric field, which leads to stronger electric dipoles when the particles polarize. This leads to higher interparticle attraction and a higher particle contact coordination number as seen in Fig. 1(a). In industrial-fluidized beds, elutriation of particles from the bed is of serious concern. As particle agglomerates are less easily elutriated than individual particles, attractive forces between polarizable, charged particles can be expected to lower elutriation, as has been found in a recent experimental study [12].

Interestingly, an asymmetric flow pattern, which takes the form of a sheetlike structure shown in Fig. 3(b), emerges in the case of highly polarized particles at large e/g values. As dipole-induced attraction takes place in the direction of the electric field (which is principally in the wall-normal direction), the sheetlike structure also forms parallel to a wall, as opposed to particle clusters typically observed in nondirectional forms of cohesion such as liquid bridges [44,45] or van der Waals forces [46]. The sharp change in the particle volume fraction variance between the meandering and sheeted regions is associated with this change in the particle flow behavior. Such sheeting of particles has been reported in industrial-fluidized bed polymerization reactors [20–22], and is undesirable from a reactor performance point of view.

In summary, electrostatic interactions due to particle charging and polarization significantly affect confined particle-laden flows. Both particle charging and polarization make meandering flows more prevalent. An asymmetric flow pattern, referred to as sheeted flow, is realized only when particle polarization is taken into consideration. Earlier studies [11,12] have used the ratio of total electrostatic forces to gravitational force to describe the system behavior where the electrostatic forces are evaluated by an expression derived by Feng [27] that combines polarization and Coulomb forces. In this study, we find that particle polarization can give rise to a qualitatively different flow behavior than a strongly charged system. Therefore, the dielectric polarization of particles should be considered independently from the Coulombic interactions, rather than attempting to lump all electrostatic influences together.

The potentially strong influence of polarization even in the absence of an externally imposed electric field reported in this study suggests that one could manipulate flows of dense assemblies of polarizable particles by an applied

field—introducing, strengthening, or weakening yield stress in the assembly and thus enabling flow control, an idea widely exploited in the context of electrorheological fluids [47].

---

*kolehma8@gmail.com

[1] D. Schmidt, R. Schmidt, and J. Dent, J. Geophys. Res. Atmos. **103**, 8997 (1998).

[2] J. F. Kok and N. O. Renno, Phys. Rev. Lett. **100**, 014501 (2008).

[3] M. D. Hogue, C. I. Calle, P. S. Weitzman, and D. R. Curry, J. Electrost. **66**, 32 (2008).

[4] K. M. Forward, D. J. Lacks, and R. M. Sankaran, Geophys. Res. Lett. **36** (2009).

[5] M. Hassani, R. Zarghami, H. Norouzi, and N. Mostoufi, Powder Technol. **246**, 16 (2013).

[6] M. Korevaar, J. Padding, M. Van Der Hoef, and J. Kuipers, Powder Technol. **258**, 144 (2014).

[7] S. Naik, S. Sarkar, B. Hancock, M. Rowland, Y. Abramov, W. Yu, and B. Chaudhuri, Powder Technol. **297**, 211 (2016).

[8] C. Pei, C.-Y. Wu, and M. Adams, Powder Technol. **304**, 208 (2016).

[9] Y. Yang, C. Zi, Z. Huang, J. Wang, M. Lungu, Z. Liao, Y. Yang, and H. Su, Powder Technol. **308**, 422 (2017).

[10] J. Kolehmainen, A. Ozel, C. M. Boyce, and S. Sundaresan, AIChE J. **63**, 1872 (2017).

[11] F. Fotovat, T. A. Alsmari, J. R. Grace, and X. T. Bi, Powder Technol. **316**, 157 (2017).

[12] F. Fotovat, J. R. Grace, and X. T. Bi, AIChE J. **63**, 1194 (2017).

[13] N. O. Renno, A.-S. Wong, S. K. Atreya, I. de Pater, and M. Roos-Serote, Geophys. Res. Lett. **30** (2003).

[14] W. Farrell, P. Smith, G. Delory, G. Hillard, J. Marshall, D. Catling, M. Hecht, D. Tratt, N. Renno, M. Desch *et al.*, J. Geophys. Res. Planets **109** (2004).

[15] T. Pähtz, H. Herrmann, and T. Shinbrot, Nat. Phys. **6**, 364 (2010).

[16] Y. Shao, M. R. Raupach, and J. F. Leys, Aust. J. Soil Res. **34**, 309 (1996).

[17] S. V. Vladimirov and K. Ostrikov, Phys. Rep. **393**, 175 (2004).

[18] I. Levchenko, K. Ostrikov, A. Rider, E. Tam, S. Vladimirov, and S. Xu, Phys. Plasmas **14**, 063502 (2007).

[19] M. Meyyappan, L. Delzeit, A. Cassell, and D. Hash, Plasma Sources Sci. Technol. **12**, 205 (2003).

[20] G. Hendrickson, Chem. Eng. Sci. **61**, 1041 (2006).

[21] D. Song and P. Mehrani, Powder Technol. **316**, 166 (2017).

[22] E. J. Markel, R. O. Hagerty, R. W. Impelman, R. B. Pannell, and C. F. Saladino (2013), U.S. Patent No. 8,378, 040 (2013).

[23] Z. L. Wang, Nature (London) **542**, 159 (2017).

[24] T. Siu, W. Pittman, J. Cotton, and T. Shinbrot, Granular Matter **17**, 165 (2015).

[25] K. R. LaMarche, F. J. Muzzio, T. Shinbrot, and B. J. Glasser, Powder Technol. **199**, 180 (2010).

[26] V. Lee, S. Waitukaitis, M. Miskin, and H. Jaeger, Nat. Phys. **11**, 733 (2015).

[27] J. Q. Feng, Phys. Rev. E **62**, 2891 (2000).

[28] J. Laurentie, P. Traoré, and L. Dascalescu, J. Electrost. **71**, 951 (2013).

[29] S. Naik, S. Saurabh, G. Vipul, H. Bruno, Y. Abramov, W. Yu, and B. Chaudhuri, Int. J. Pharm. **491**, 58 (2015).

[30] J. Kolehmainen, P. Sippola, O. Raitanen, A. Ozel, C. M. Boyce, P. Saarenrinne, and S. Sundaresan, Chem. Eng. Sci. **173**, 363 (2017).

[31] See Supplemental Material at http://link.aps.org/supplemental/10.1103/PhysRevLett.121.124503 for simulation details, which includes Refs. [32–39].

[32] T. B. Anderson and R. Jackson, Ind. Eng. Chem. Fundam. **6**, 527 (1967).

[33] P. Pepiot and O. Desjardins, Powder Technol. **220**, 104 (2012).

[34] A. Ozel, J. Kolehmainen, S. Radl, and S. Sundaresan, Chem. Eng. Sci. **155**, 258 (2016).

[35] Z. Zhou, S. Kuang, and A. Yu, J. Fluid Mech. **661**, 482 (2010).

[36] C. Kloss, C. Goniva, A. Hager, S. Amberger, and S. Pirker, Prog. Comput. Fluid Dyn. **12**, 140 (2012).

[37] C. Goniva, C. Kloss, N. Deen, J. Kuipers, and S. Pirker, Particuology **10**, 582 (2012).

[38] K. Johnson, *Contact Mechanics* (Cambridge University Press, Cambridge, 1987).

[39] A. Renzo and F. P. Di Maio, Chem. Eng. Sci. **59**, 525 (2004).

[40] J. Capecelatro and O. Desjardins, J. Comput. Phys. **238**, 1 (2013).

[41] P. Cundall and O. Strack, Geotechnique **29**, 47 (1979).

[42] C. Wen and Y. H. Yu, Chem Eng Prog, Symp Ser **62**, 100 (1966).

[43] J. Kolehmainen, A. Ozel, C. M. Boyce, and S. Sundaresan, AIChE J. **62**, 2282 (2016).

[44] V. Richefeu, M. S. El Youssoufi, and F. Radjai, Phys. Rev. E **73**, 051304 (2006).

[45] C. M. Boyce, A. Ozel, J. Kolehmainen, S. Sundaresan, C. A. McKnight, and M. Wormsbecker, AIChE J. **63**, 2520 (2017).

[46] Y. Gu, S. Chialvo, and S. Sundaresan, Phys. Rev. E **90**, 032206 (2014).

[47] T. C. Halsey, Science **258**, 761 (1992).